

Sound absorption enhancement in poro-elastic materials in the viscous regime using a mass–spring effect

Peer-reviewed author version

Ahsani , S.; Claeys , C.; Zielinski, T. G.; Jankowski , L.; Scarpa, F.; Desmet, W. & DECKERS, Elke (2021) Sound absorption enhancement in poro-elastic materials in the viscous regime using a mass–spring effect. In: JOURNAL OF SOUND AND VIBRATION, 511 (Art N° 116353).

DOI: 10.1016/j.jsv.2021.116353

Handle: <http://hdl.handle.net/1942/36546>

# Sound absorption enhancement in poro-elastic materials in the viscous regime using a mass-spring effect

S. Ahsani<sup>a,b,c</sup>, C. Claeys<sup>a,b</sup>, T. G. Zieliński<sup>e</sup>, Ł. Jankowski<sup>e</sup>, F. Scarpa<sup>c,f</sup>, W. Desmet<sup>a,b</sup>, E. Deckers<sup>b,d</sup>

<sup>a</sup>*KU Leuven, Department of Mechanical Engineering, Division LMSD, Celestijnenlaan 300 - box 2420, Heverlee, Belgium*

<sup>b</sup>*DMMS Lab, Flanders Make, Heverlee, Belgium*

<sup>c</sup>*Bristol Composites Institute (ACCIS), University of Bristol, BS8 1TR Bristol, UK*

<sup>d</sup>*KU Leuven, Campus Diepenbeek, Mechanical Engineering Technology, Wetenschapspark 27, 3590 Diepenbeek*

<sup>e</sup>*Institute of Fundamental Technological Research, Polish Academy of Sciences, Pawinskiego 5B, 02-106 Warsaw, Poland*

<sup>f</sup>*Dynamics and Control Research Group (DCRG), University of Bristol, BS8 1TR Bristol, UK*

---

## Abstract

This paper investigates the mechanisms that can be used to enhance the absorption performance of poro-elastic materials in the viscous regime. It is shown that by adding small inclusions in a poro-elastic foam layer, a mass-spring effect can be introduced. If the poro-elastic material has relatively high viscous losses in the frequency range of interest, the mass-spring effect can enhance the sound absorption of the foam by introducing an additional mode in the frame and increasing its out-of-phase movement with respect to the fluid part. Moreover, different effects such as the trapped mode effect, the modified-mode effect, and the mass-spring effect are differentiated by decomposing the absorption coefficient in terms of the three energy dissipation mechanisms (viscous, thermal, and structural losses) in poro-elastic materials. The physical and geometrical parameters that can amplify or decrease the mass-spring effect are discussed. Additionally, the influence of the incidence angle on the mass-spring effect is evaluated and a discussion on tuning the inclusion to different target frequencies is given.

*Keywords:* Meta-poro-elastic material, Biot-Allard poroelastic model, Mass-spring effect, Viscous regime

---

## 1. Introduction

Porous materials are widely used as acoustic absorbers. They are inefficient and bulky solutions at low frequencies since they only exhibit perfect or near perfect absorption at the so-called quarter-wavelength resonance frequency. Multi-layering is a well-known and traditional approach to improve the efficiency of porous materials at low frequencies, which is again limited by the allowable thickness [1]. Researchers

---

*Email address:* [sepide.ahsani@kuleuven.be](mailto:sepide.ahsani@kuleuven.be) (S. Ahsani)

28 have recently addressed this issue using unconventional solutions, such as embedding inclusions in the  
29 foam to create macroscopically inhomogeneous porous materials. Groby et al. [2] investigated the effect of  
30 low/high contrast inclusions in terms of both modal behavior and the acoustic response. They showed that,  
31 by considering a high contrast inclusion, the modified mode of the porous layer can be induced, leading to  
32 an increase in the absorption. The modified mode of the porous layer is defined as modes with evanescent  
33 waves in the ambient fluid and propagative waves in the porous layer, hence leading to energy entrapment in  
34 the porous layer. Moreover, they showed that the modified mode frequency has a positive frequency offset  
35 with respect to the natural frequency of the homogeneous layer. This frequency offset is dependent on the  
36 periodicity length and the inclusion dimension. Later on, Groby et al. [3] used periodic rigid inclusions to  
37 improve the absorption of a rigid-frame foam layer under the quarter-wavelength limit. They demonstrated  
38 that if the size of the inclusion is comparable to the acoustic wavelength, energy can be trapped between the  
39 inclusion and the rigid backing, and therefore be dissipated through viscous and thermal effects. Moreover,  
40 they showed that perfect or near perfect absorption due to this trapped mode can be achieved above the  
41 decoupling frequency, i.e. in the inertial regime. Their findings led Lagarrigue et al. [4] to create a meta-  
42 porous layer using a periodic array of rigid split-ring resonators (analyzed in the air by Krynkin et al. [5])  
43 which, when used as inclusions in a rigid-frame foam, improve the absorption by combining the trapped  
44 mode phenomena and the resonance of the fixed rigid split-ring resonators. Additionally, in Ref. [6] authors  
45 extended the idea to a 3D configuration by using Helmholtz resonators to enhance the absorption coefficient  
46 of a rigid-frame porous material in the inertial regime due to Helmholtz resonances and the trapped mode  
47 effect. In a more recent work, Weisser et al. [7] investigated the concept of a meta-poro-elastic system below  
48 the decoupling frequency. They considered two different types of elastic inclusions; a homogeneous and  
49 relatively stiff inclusion made of steel or plexiglass, and a thin-wall resonant shell inclusion filled with air,  
50 having a pronounced mode in the lower frequency regime. The stiffer inclusion, made of rubber, resulted in  
51 similar performance as a rigid inclusion in the rigid-frame foam layer [3]. The more flexible shell inclusion,  
52 however, led to additional absorption enhancement at low frequencies due to the flexural modes of the shell.  
53 Zieliński [8] investigated numerically the effect of introducing periodic point-mass inclusions in a poro-  
54 elastic layer. He showed that the absorption performance of poro-elastic materials can be improved by the  
55 so-called mass-spring effect, where the foam under the mass inclusions acts as a spring, creating a mass-  
56 spring system with a certain resonance frequency depending on the mass and location of the inclusion. This  
57 effect was shown experimentally in Ref. [9] in the context of transmission loss improvement when multiple

58 mass inclusions were added to a foam layer. In view of exploiting frame vibrations, active meta-poro-elastic  
59 layers with piezoelectric inclusions were proposed by Zieliński in Ref. [10] to actively modify the vibrations  
60 of the elastic skeleton of the poro-elastic layer in order to increase sound absorption. This idea was further  
61 studied in Ref. [11], where small passive inclusions were added to enhance the active effect. Recently, the  
62 use of resonant behavior at the micro-scale to improve the acoustic performance of poro-elastic materials  
63 has been investigated and discussed in Refs. [12, 13], where micro-scale resonators are embedded in the  
64 pores of the poro-elastic material. These resonators consist of a cantilever beam with added mass at the tip.  
65 Lewińska et al. have demonstrated that the visco-thermal dissipation is increased by the local resonant effect  
66 and this is due to the complex coupling between the solid and fluid phase. Moreover, they have shown that  
67 the micro-resonators attenuate the fast compressional wave and that the amount of this attenuation depends  
68 on the pore size, the opening ratio (area fraction of the opening in the pores), and the viscosity of the fluid  
69 in the pores.

70 All the works mentioned above and many others like Refs. [14, 15, 16, 17, 18, 19] show great potential  
71 in meta-porous and meta-poro-elastic systems as an innovative solution to create narrow or broadband ab-  
72 sorbers at low frequencies. However, the contributions were mainly focused on improving the absorption  
73 performance of foams with a low decoupling frequency and thus acting in the inertial regime. The current  
74 work focuses on improving the absorption performance of poro-elastic materials with a high decoupling fre-  
75 quency, for which the frame vibration cannot be neglected, by exploiting the resonant behavior induced by  
76 the mass-spring effect. Therefore, this paper investigates meta-poro-elastic systems with inclusions that are  
77 modeled under different assumptions, namely rigid and motionless, point-mass, and elastic, to distinguish  
78 the mechanisms that influence the acoustic response. With this gained knowledge, configurations can be  
79 designed that achieve absorption enhancement over a broader frequency range by combining these mech-  
80 anisms. In this work, the Biot theory [20, 21] of poro-elastic materials is used to account for the frame's  
81 motion. Additionally, the criteria under which the mass-spring effect can be achieved are discussed in detail.  
82 Furthermore, a general guideline is given to tune the mass-spring absorption peak to a targeted frequency.

83 This paper is structured as follows. Section 2 explains the modeling technique used for the poro-elastic  
84 material and the inclusions. Section 3 includes three main parts. The first part discusses different structural  
85 resonant behaviors in meta-poro-elastic systems, while the second one dives deeper into the concept of the  
86 mass-spring effect. The third part concludes the section with a qualitative study on the tunability of the  
87 mass-spring effect.

88 **2. Problem formulation**

89 This section consists of four parts. The first part describes the problem configuration. The model used  
 90 for the poro-elastic material is detailed in the second part. The third part explains the models used for the  
 91 inclusion and the fourth part details the field variables representation in a periodic configuration.

92 *2.1. Problem configuration*

93 The cases studied in this paper, depicted in Figure 1, are assumed to be invariant in the  $z$ -direction. The  
 94 studied cases include an acoustic domain ( $\Omega_a$ ), being the ambient fluid, and a poro-elastic domain ( $\Omega_p$ ) with  
 95 a thickness  $L_y$  and a rigid backing on the bottom. The poro-elastic and acoustic domains are periodic in  
 96 the  $x$ -direction with a unit cell characteristic length of  $L_x$ . The  $x$ -direction periodicity is accounted for by  
 97 using periodic field variables, as described in Section 2.4. Moreover, meta-poro-elastic cases are considered  
 98 by introducing a rod inclusion of radius  $r$  at the location of  $(\frac{L_x}{2}, y)$ . Additionally, the system is constrained  
 99 in the  $y$ -direction at the base end and is impinged by a plane wave at the top end with an oblique incidence  
 100 angle  $\theta$ .

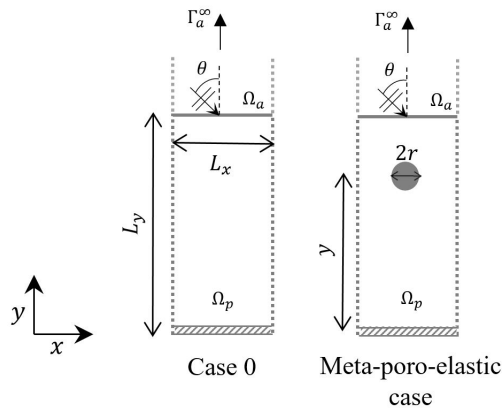


Figure 1: Schematic view of the cases considered in this paper.

101 *2.2. Poro-elastic material modeling*

102 The theory of Biot [20, 21, 22] is used to model the poro-elastic material such that the visco-elasticity  
 103 and motion of the frame are taken into account. This is to ensure that viscous effects are correctly accounted  
 104 for when analyzing the absorption behavior below the decoupling frequency.

The mixed  $\mathbf{u}$ - $p$  formulation [23, 24] of the Biot poro-elasticity theory [20, 21, 25] is used, in which  
 the primary field variables are the solid phase displacements  $\mathbf{u}$  and the fluid pressure in the pores  $p$ . This

formulation is valid for harmonic motion, and is described by the following set of coupled solid and fluid phase equations of motion:

$$\nabla \cdot \boldsymbol{\sigma}(\mathbf{u}) + \omega^2 \tilde{\rho} \mathbf{u} + \tilde{\gamma} \nabla p = \mathbf{0}, \quad (1)$$

$$\nabla^2 p + \omega^2 \frac{\tilde{\rho}_{22}}{\tilde{R}} p - \omega^2 \tilde{\gamma} \frac{\tilde{\rho}_{22}}{\phi^2} \nabla \cdot \mathbf{u} = 0, \quad (2)$$

105 with

$$\tilde{\rho} = \tilde{\rho}_{11} - \frac{\tilde{\rho}_{12}^2}{\tilde{\rho}_{22}}, \quad \tilde{\gamma} = \phi \left( \frac{\tilde{\rho}_{12}}{\tilde{\rho}_{22}} - \frac{\tilde{Q}}{\tilde{R}} \right). \quad (3)$$

106 Here,  $\phi$  is the porosity, while  $\tilde{\rho}_{11}$ ,  $\tilde{\rho}_{22}$ , and  $\tilde{\rho}_{12}$  are the effective densities which take into account the fact that  
 107 the relative flow through the pores is not uniform and that there is a visco-inertial interaction between the  
 108 solid and fluid phases leading to energy dissipation induced by the relative motion of the two phases [23, 26].  
 109 Furthermore,  $\tilde{Q}$  is a coupling coefficient between the dilatation and stress of the two phases, while  $\tilde{R}$  is the  
 110 bulk modulus of the fluid phase. The second-order tensor  $\boldsymbol{\sigma}(\mathbf{u})$ , which appears in the solid phase equation  
 111 of motion (1), describes the stresses in the elastic frame in vacuum and depends only on the solid phase  
 112 displacement, namely,

$$\boldsymbol{\sigma} = \hat{A} (\nabla \cdot \mathbf{u}) \mathbf{I} + \tilde{N} (\nabla \mathbf{u} + \nabla^T \mathbf{u}), \quad (4)$$

113 where  $\mathbf{I}$  is the second-order identity tensor, while  $\hat{A}$  and  $\tilde{N}$  are the Lamé coefficients of the visco-elastic  
 114 frame. When  $\nu$ ,  $N$ , and  $\eta$  denote the bulk Poisson ratio, shear modulus, and loss factor of the frame,  
 115 respectively, then:  $\tilde{N} = N(1 + i\eta)$  and  $\hat{A} = \frac{2\nu}{1-2\nu} \tilde{N}$ . Note that both these coefficients are complex-valued  
 116 because of the visco-elastic behaviour of the frame leading to structural energy losses.

117 The formulae for the effective densities  $\tilde{\rho}_{11}$ ,  $\tilde{\rho}_{22}$ , and  $\tilde{\rho}_{12}$  can be found, for example, in Refs. [22, 23, 27].  
 118 They depend not only on the (homogenised bulk) densities of solid and fluid phases but also on a frequency-  
 119 dependent viscous damping coefficient [22, 27]:

$$\tilde{b} = i\omega \phi \rho_a (\tilde{\alpha}(\omega) - \alpha_\infty), \quad (5)$$

120 which accounts for viscous interaction forces. This coefficient is related to the fluid phase density  $\phi \rho_a$   
 121 (here,  $\rho_a$  is the density of air, i.e. the actual fluid in pores) and to the difference between the frequency-  
 122 dependent viscous dynamic tortuosity  $\tilde{\alpha}(\omega)$  and kinematic tortuosity  $\alpha_\infty$  of the porous material. Johnson et

123 al. [28] proposed a semi-phenomenological model for  $\tilde{\alpha}(\omega)$  depending on **the** transport parameters of porous  
 124 material, viz. the viscous permeability (or airflow resistivity  $\sigma$ ), porosity  $\phi$ , kinematic tortuosity  $\alpha_\infty$ , and  
 125 viscous characteristic length  $\Lambda$ . The effective moduli  $\tilde{Q}$  and  $\tilde{R}$  can be computed from formulae provided  
 126 in [25, 22, 23, 24]. In particular, they depend on the dynamic (i.e. frequency-dependent) effective bulk  
 127 modulus of air-saturated rigid porous medium for which a semi-phenomenological model was proposed by  
 128 Champoux and Allard [29]. In that way, the Biot-Allard model [22, 27, 28, 29] for sound propagation and  
 129 absorption in poro-elastic materials is applied in this work **for** all analyses assuming a visco-elastic frame,  
 130 while the Johnson-Champoux-Allard (JCA) equivalent-fluid model [22, 28, 27] is occasionally used for  
 131 comparison when the frame is assumed rigid.

### 132 2.3. Inclusion modeling

133 In this paper, three different ways are used to model the inclusion in order to isolate different effects, i.e.  
 134 the mass-spring effect, the trapped mode effect, and the effect of the modified mode of the frame, leading to  
 135 an increase in the absorption coefficient in dedicated frequency ranges.

#### 136 2.3.1. Point- mass inclusion

137 The first and the most simple approach is to consider the inclusion as a concentrated mass ( $m_0$ ), **dis-**  
 138 **tinguishing** the mass-spring effect from the others. Therefore, an inertial weak contribution is added to the  
 139 variational formulation of the poro-elastic material [8]:

$$\mathcal{WF}_p + \int_{\Omega_p} \omega^2 m_0 \delta(\mathbf{x} - \mathbf{x}_0) \mathbf{u} \cdot \mathbf{w} d\Omega_p = 0. \quad (6)$$

140  $\mathcal{WF}_p$  is the weak form for a poro-elastic material in the domain  $\Omega_p$ ,  $m_0$  is the point-mass of the inclusion  
 141 concentrated at the point  $\mathbf{x}_0$ ,  $\delta$  is the Dirac delta function, and  $\mathbf{w}$  is the test function for  $\mathbf{u}$ .

#### 142 2.3.2. Rigid and motionless inclusion

143 In the second approach, to exclude the effect due to the motion of the inclusion (resonance behaviour),  
 144 and therefore, to identify the effect induced by the inclusion size and geometry (trapped mode effect and  
 145 modified mode of the frame), the inclusion of finite size is simply considered rigid and motionless. To  
 146 model this, boundary conditions for a rigid and impervious wall are applied on the inclusion surface  $\Gamma_{p-r}$ ,  
 147 which means that the solid phase displacements and normal displacements of **the** fluid phase are zero  
 148 on  $\Gamma_{p-r}$  [30, 24]. Since the second condition (which describes the fact that there is no relative mass flux

149 across the impervious boundary) is naturally handled in the enhanced  $\mathbf{u}$ - $p$  formulation [24] (i.e. the corre-  
 150 sponding surface integral in the weak formulation is zero), only the kinematic condition for the solid phase  
 151 displacements [24], i.e.  $\mathbf{u} = \mathbf{0}$  on  $\Gamma_{p-r}$ , needs to be included.

### 152 2.3.3. Elastic inclusion

153 In the third approach, the coupling between different effects (inertial, trapped mode effect, and modified  
 154 mode of the frame) is taken into account by modeling the inclusion as an isotropic elastic domain and as-  
 155 suming that the poro-elastic layer is glued to the surface of this domain. Therefore, coupling conditions are  
 156 applied on the interface  $\Gamma_{p-e}$  between the poro-elastic and elastic domains, namely [30, 24]: the continuity  
 157 of the total normal stresses at the interface, no relative mass flux across the impervious interface, and the  
 158 continuity of the solid phase displacement vector of poro-elastic medium  $\mathbf{u}$  and the elastic displacement  
 159 vector  $\mathbf{u}^e$  of the inclusion. However, since in the  $\mathbf{u}$ - $p$  formulation the coupling between the poro-elastic  
 160 and elastic media is natural, only the kinematic coupling condition, i.e.  $\mathbf{u} = \mathbf{u}^e$  on  $\Gamma_{p-e}$ , has to be explicitly  
 161 imposed [24].

### 162 2.4. Field representations

163 As the problem is periodic in space and is excited by a plane wave, the field variables are considered to  
 164 be periodic (in the  $x$ -direction) in the poro-elastic domain  $\Omega_p$ , acoustic domain  $\Omega_a$ , and elastic domain  $\Omega_e$ .  
 165 Therefore, each field variable  $W$  satisfies the Floquet-Bloch relation [31]:

$$W(\mathbf{x} + \mathbf{d}) = W(\mathbf{x}) \exp(i\tilde{\mathbf{k}} \cdot \mathbf{d}), \quad (7)$$

166 where  $\mathbf{d}$  is the spatial periodicity and  $\tilde{\mathbf{k}} = \{\tilde{k}_1, \tilde{k}_2, 0\}$  is the in-plane component of the incident wave number.  
 167 In our case  $\mathbf{d} = \{d_1, 0, 0\}$ , where  $d_1 = L_x$ . Then, the periodicity in solid, acoustic, and poro-elastic **domains**  
 168 can be taken into account by substituting the field variables  $W$  in the governing equations of each domain  
 169 by their periodic generalisations [32]  $\hat{W}(\mathbf{x}) = W(\mathbf{x}, \tilde{\mathbf{k}}) \exp(i\tilde{\mathbf{k}} \cdot \mathbf{x})$ . The corresponding weak forms associated  
 170 with the dynamic equations of each domain are given in Appendix A. Moreover, the mutual interaction  
 171 between the acoustic and poro-elastic **domains** is ensured in two steps [30]. In the first step, the continuity  
 172 of the pressure at the interface of the two domains is applied. In the second step, the pressure in the acoustic  
 173 domain at the interface is considered as a surface traction force on the solid phase of the poro-elastic domain,  
 174 while the structural acceleration due to the solid phase of the poro-elastic domain is applied on the acoustic  
 175 domain pressure. Readers are referred to [33] for the mathematical expression of the acoustic-poro-elastic

176 coupling condition. Furthermore, the radiating boundary condition is applied by using the Floquet mode  
177 decomposition, as explained in [31].

### 178 **3. Results and discussion**

179 This section is divided into three main parts. In the first part, the discussion focuses on the resonant  
180 behaviors, namely the mass-spring resonance and the frame resonance in meta-poro-elastic materials, by in-  
181 vestigating three cases. The differences between the modified mode and the mass-spring effects are pointed  
182 out by analyzing the decomposed absorption coefficients in terms of three energy dissipation **mechanisms**,  
183 i.e. viscous, thermal, and structural losses [27]. In the second part, the mass-spring effect is studied in de-  
184 tail. The investigation is mainly focused on the conditions under which the mass-spring effect is amplified  
185 or disappears. These limits are evaluated, taking into account the inclusion mass and size, as well as **the**  
186 poro-elastic material properties. In the third part, an optimization routine is used to derive optimum values  
187 for geometrical parameters of the inclusion such that the mass-spring effect is obtained at a specified fre-  
188 quency. The evolution of these parameters over frequency is then analyzed to derive a qualitative guideline  
189 to design a meta-poro-elastic material for a targeted frequency.

#### 190 *3.1. Resonant behavior in poro-elastic materials*

191 This section investigates the induced resonant behaviors in the poro-elastic skeleton due to the added  
192 inclusions and how they improve the absorption performance. Two resonant behaviors are studied: the  
193 modified mode of the frame and the mass-spring effect. The former refers to the first mode of the frame  
194 and how the vibration pattern and occurring frequency are influenced **by** the periodicity introduced in the  
195 system and the added stiffness/mass by the inclusion. The latter is a new mode of the system due to the  
196 mass of the inclusion which is resonating on the stiffness of the poro-elastic frame, hence constituting a  
197 mass-spring system.

198 The resonant behavior in the poro-elastic material is studied by considering three cases. The first case  
199 is the reference case (case 0) and is composed of a homogeneous (i.e. without inclusions) foam layer with a  
200 thickness of  $L_y = 24$  mm set on a rigid backing. In the second and third cases, a steel rod inclusion with a  
201 radius of  $r = 0.4$  mm is introduced at  $y_A = 4$  mm (case A) and  $y_B = 20$  mm (case B) from the rigid backing  
202 respectively. In both of these cases, the width of the periodic cell is  $L_x = 8$  mm, which is the distance along  
203 the  $x$ -axis between the periodically embedded inclusions. In all analyses, Biot's poro-elasticity theory is  
204 used to model the poro-elastic foam, where the Johnson-Champoux-Allard (JCA) [22, 28, 29] model is

205 used to determine the effective density and bulk modulus for the air saturating the pores. The required  
 206 Biot-JCA parameters used in all analyses are those for a polyurethane foam given in Table 1, where  $N$ ,  $\eta$   
 207 are the shear modulus and loss factor of the frame,  $\nu$  is the bulk Poisson ratio,  $\rho_1$  is the bulk density,  $\phi$  is the  
 208 porosity,  $\alpha_\infty$  is the tortuosity,  $\Lambda$ ,  $\Lambda'$  are the viscous and thermal characteristic lengths, and  $\sigma$  is the airflow  
 209 resistivity. These parameters are taken from Ref. [23]. Note also that the transport parameters  $\phi$ ,  $\alpha_\infty$ ,  $\Lambda$ ,  
 210  $\Lambda'$ , and  $\sigma$  are used by the JCA model of equivalent fluid when (for comparison) the foam is modeled as a  
 211 rigid-frame porous material.

$N$ (kPa)	$\eta$	$\nu$	$\rho_1$ (kg/m <sup>3</sup> )	$\phi$	$\alpha_\infty$	$\Lambda$ ( $\mu\text{m}$ )	$\Lambda'$ ( $\mu\text{m}$ )	$\sigma$ (Pa·s/m <sup>4</sup> )
55	0.055	0.3	31	0.97	2.52	37	119	87000

Table 1: The Biot parameters of the foam [23]

212 COMSOL Multiphysics is used to discretize and solve the Finite Element (FE) analyses for each case.  
 213 These problems have been implemented using the weak formulations given in Appendix A. Mesh conver-  
 214 gence studies have been performed for all cases resulting in FE meshes consisting of 893, 1006, and 1275  
 215 quadratic elements, yielding 6126, 10197, and 14751 DOFs, for the meta-poro-elastic system with the rigid  
 216 inclusion model, point-mass inclusion model, and elastic inclusion model, respectively.

### 217 3.1.1. Sound absorption of the homogeneous poro-elastic layer

218 The total sound absorption and the corresponding decomposed absorption coefficients for case 0, with  
 219 normal angle of incidence, are shown in Figure 2. It can be seen that simultaneously a dip in total absorption  
 220 and viscous losses, as well as a peak in the structural losses, appear at approximately 820 Hz. This frequency  
 221 corresponds to the resonance frequency of the frame with rigid backing [22], which is calculated as follows:

$$f_r = \frac{1}{4L_y} \sqrt{\frac{K_c}{\rho_1}}, \quad (8)$$

222 where  $K_c = \frac{2(1-\nu)N}{(1-2\nu)}$ . Since the structural losses directly correspond to the amount of strain in the solid phase  
 223 of poro-elastic material, the structural loss at the resonance frequency of the frame is increased. However,  
 224 viscous losses depend on the viscous coupling coefficient, which is dependent on foam properties, and the  
 225 out-of-phase movement of the fluid and solid phase. The latter explains the dip at  $f_r$  (in-phase movement of  
 226 the fluid in the pores and the frame), and also the peak above  $f_r$  (anti-phase displacement of the frame and  
 227 the fluid).

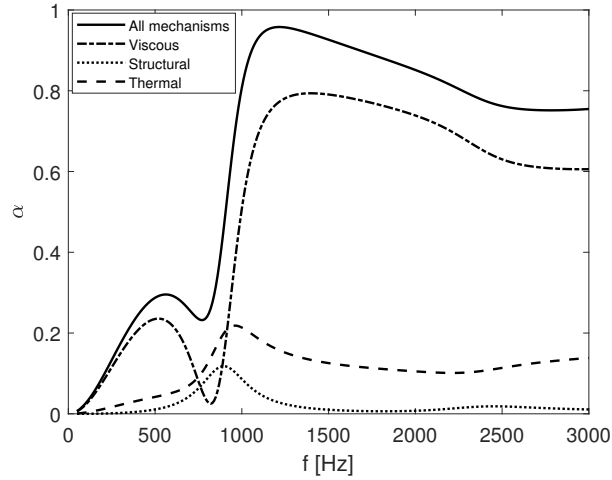


Figure 2: Partial absorption coefficient for different dissipation mechanisms for the poro-elastic foam without inclusions.

228 Another important characteristic of poro-elastic materials is the decoupling frequency  $f_c$ , at which the  
 229 transition from viscous to inertial regime occurs. The harmonic motion of the fluid phase does not excite  
 230 the frame above this frequency [22], i.e. the two phases are decoupled and the energy is dissipated mainly  
 231 due to the inertial effect **as opposed to** the viscous drag between the two phases. The decoupling frequency  
 232 is commonly defined as follows [21]:

$$f_c = \frac{\phi \sigma}{2\pi\rho_a}, \quad (9)$$

233 where  $\rho_a$  is the density of air. It should be noted that above this frequency, the rigid frame assumption  
 234 is valid and therefore the equivalent fluid model predicts the behavior of the poro-elastic layer with good  
 235 accuracy. Even below  $f_c$ , for poro-elastic materials with sufficiently stiff (rigid) skeleton, no significant  
 236 vibrations will be induced in the skeleton by airborne acoustic waves.

237 It is worth mentioning that other criteria can be used to identify the decoupling frequency such as the  
 238 inverse quality factor [34] in **the** case of foams with very low viscous characteristic length. The decoupling  
 239 frequency for the type of foam we are targeting (foams with **a** high value of flow resistivity) is at high  
 240 frequencies, more specifically for the foam used in this work the decoupling frequency is at 11.2 kHz.  
 241 Therefore, there is a significant deviation of the equivalent fluid model with respect to the theory of Biot in  
 242 the studied frequency range, see Figure 3.

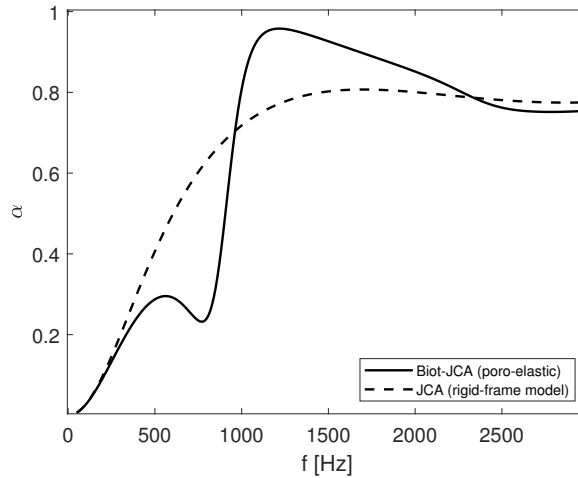


Figure 3: Absorption coefficients calculated for the homogeneous poro-elastic layer using the Biot-JCA (i.e. Biot-Allard) model and for the corresponding rigid-frame porous layer calculated using the JCA model of equivalent fluid.

### 243 3.1.2. Sound absorption of meta-poro-elastic systems in case of normal incidence angle

244 In this part, the (partial) absorption coefficients of case A and case B are calculated considering the three  
 245 different modeling techniques detailed in Section 2.3 to distinguish different resonant behaviors, i.e. the  
 246 mass-spring and modified mode effects. Below, the results corresponding to the different ways to model the  
 247 inclusion are discussed, i.e. first for case A and then for case B. **Afterward**, the resonant behaviors induced  
 248 in case A and case B due to the mass-spring system are compared to each other. These results are depicted  
 249 in Figure 4. Moreover, the absorption coefficient of case 0 is recalled for comparison to have a view on the  
 250 effect of inclusion on the acoustic response.

#### 251 I. Different inclusion modeling techniques: Case A

252 The results are discussed in two steps. The first **step** considers the absorption coefficient corresponding to  
 253 the model that assumes a motionless inclusion. The second step explains the results that take into account  
 254 the inclusion motion.

- 255 • **Rigid and motionless inclusion model** It can be seen that the absorption coefficient obtained using  
 256 the rigid and motionless inclusion model is almost identical to the one obtained for case 0 (cf. Figure 4  
 257 (a)) with a slight shift of the resonance frequency of the frame to a higher frequency (i.e. from 820 Hz  
 258 to 910 Hz). This indicates that the rigid and motionless inclusion stiffens the skeleton, causing the  
 259 first mode of the frame to be shifted upwards in frequency. The stiffening of the foam is due to the

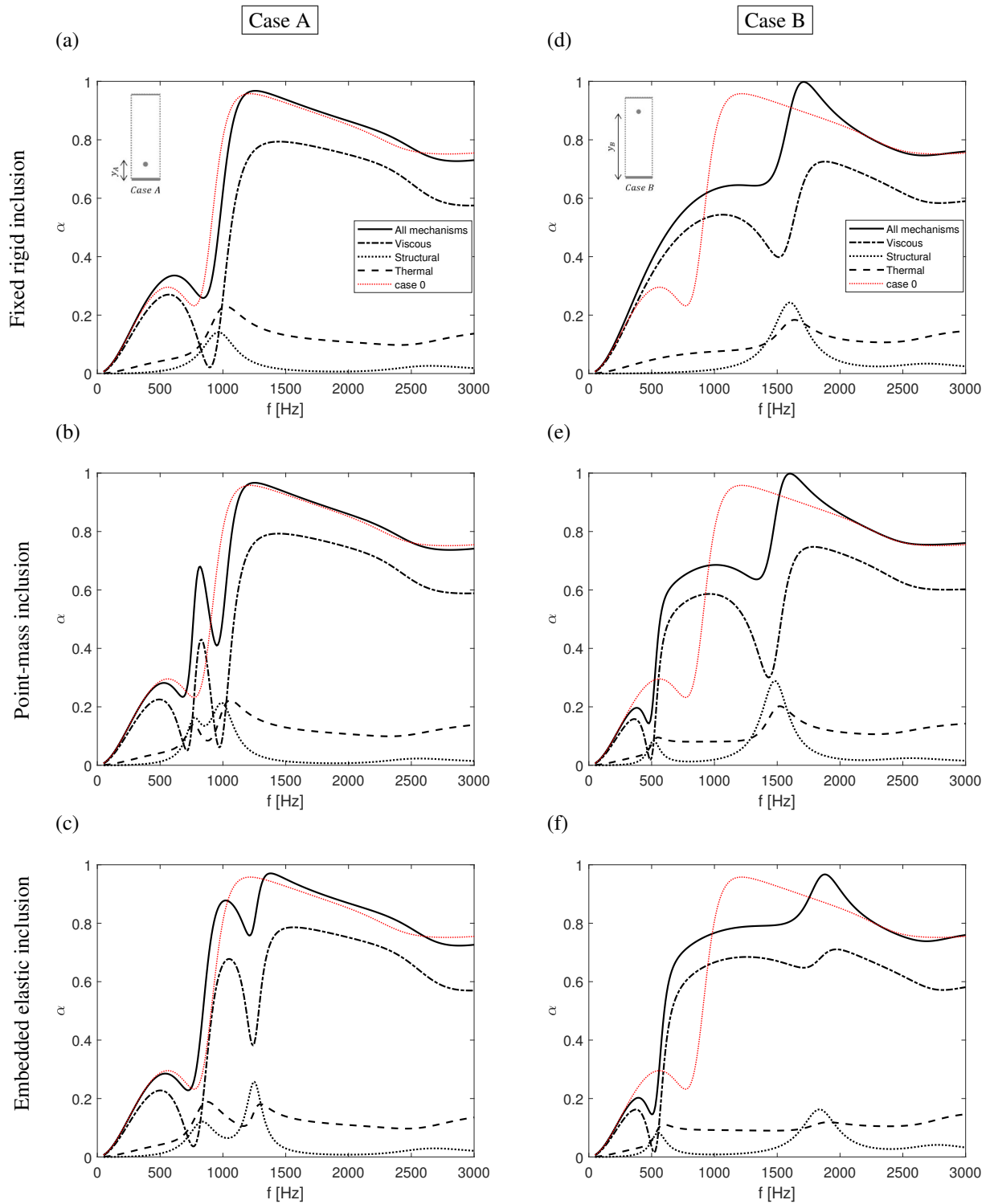


Figure 4: Total and partial absorption coefficients for case A (a,b,c) and case B (d,e,f), related to different dissipation mechanisms in the poro-elastic layer with the inclusion modeled as rigid (a,d), point mass (b,e) or elastic (c,f).

260 fact that the inclusion is modeled only by constraining the foam, and since the fixed rigid inclusion is  
 261 located very close to the rigid backing, it results in an extended area of rigid-like boundary condition.

262 • *Point-mass and elastic model* The same observation does not hold for the point-mass inclusion  
 263 (see Figure 4(b)) or the elastic inclusion (see Figure 4(c)), as there is clearly an additional peak in  
 264 the absorption coefficient. This peak is lower in frequency and is more localised in the point-mass  
 265 model as compared to the elastic inclusion model since in the point-mass model only the inertial  
 266 effect is considered while the elastic model also accounts for the size effect. Additionally, we would  
 267 like to draw the reader’s attention to the two peaks in structural losses (see Figure 4(b),(c)), which  
 268 indicate two resonance frequencies in the system. These peaks are at 770 Hz and 980 Hz for the  
 269 point-mass inclusion, and they are at 840 Hz and 1250 Hz for the elastic inclusion. To identify the  
 270 mass-spring resonance and the modified mode, the real part of the vertical component of the fluid and  
 271 solid displacements ( $v$  and  $v^f$ ) of case A with point-mass inclusion are evaluated at the frequencies  
 272 of the total absorption peaks induced by the out-of-phase motion excited after the two structural loss  
 273 peaks, see Figure 5. The vibration pattern of the frame at 820 Hz clearly presents a localized motion  
 274 around the inclusion, while at 1250 Hz a modeshape of the skeleton modified due to the presence of  
 275 the inclusion addition is noticeable. This indicates that the first structural loss peak is induced by the  
 mass-spring resonance.

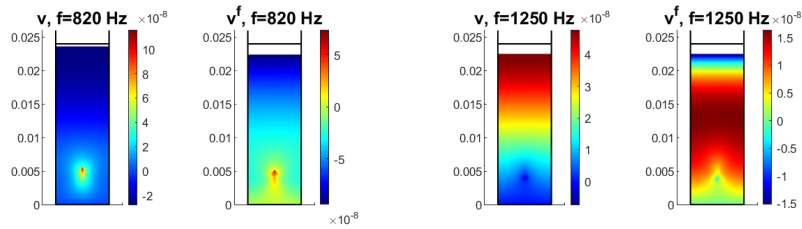


Figure 5: The displacement field (with  $v$  referring to the solid displacement along  $y$ -axis and  $v^f$  referring to the fluid displacement in the same direction) of case A with point-mass inclusion at  $f = 820$  Hz (left), and  $f = 1250$  Hz (right). These frequencies refer to the peaks in the total absorption coefficient after the mass-spring and frame resonances, respectively.

276

## 277 II. Different inclusion modeling techniques: Case B

278 The acoustic response related to different inclusion models is discussed for case B in the same manner as  
 279 for case A.

- 280 • *Rigid and motionless inclusion model* As it is observable from Figure 4, the results obtained using  
 281 the model with fixed (i.e. motionless) rigid inclusion differ significantly from those of case 0 because  
 282 the longer distance between the inclusion and the rigid backing (as compared to case A) leads to a  
 283 shift in the frame resonance frequency to higher frequencies. Therefore, the peak appearing in the  
 284 total absorption and the partial structural absorption for the case with fixed rigid inclusion is simply  
 285 due to the modification of the mode of the frame.
- 286 • *Point-mass and elastic model* For these models, a similar behavior (as in case A) is observed in case  
 287 **B. Specifically**, the point-mass and elastic inclusion models both exhibit two peaks in structural losses  
 288 **resulting from the mass-spring system and the modified mode of the frame, respectively**. Again, this  
 289 can be confirmed by visualizing the displacement fields at the total absorption peaks induced by these  
 effects and comparing them to each other, see Figure 6.

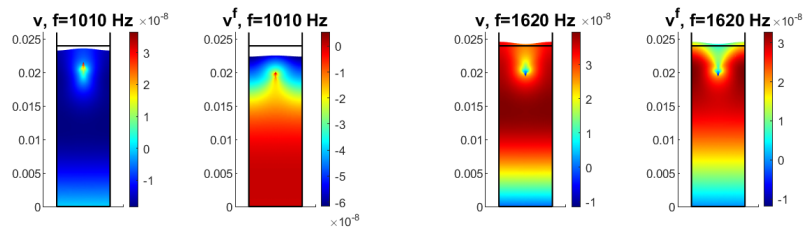


Figure 6: The displacement (with  $v$  referring to the solid displacement along  $y$ -axis and  $v^f$  referring to the fluid displacement in the same direction) of case B with point mass inclusion at  $f = 1010$  Hz (left), and  $f = 1620$  Hz (right). These frequencies refer to the peak in the total absorption coefficient after the mass-spring and frame resonance.

290

291 On the one hand, the absorption enhancement for case B is achieved over a broader frequency band  
 292 as compared to case A for **both** the embedded elastic and point-mass inclusions due to the combined  
 293 mass-spring and modified mode effects. On the other hand, the resonance frequency of the frame is  
 294 shifted to higher frequencies as compared to case A and case 0 and the system reaches a perfect or  
 295 almost perfect absorption at higher frequencies. As a result, the absorption coefficient is reduced at  
 296 some higher frequencies in the meta-poro-elastic system as compared to case 0. For example, the  
 297 maximum absorption for case 0 is 0.95 at 1140 Hz and is reduced at this frequency to 0.78 when an  
 298 elastic inclusion is added, cf. Figure4(f).

299 *III. Comparison of mass-spring resonance in case A and case B*

300 When comparing the resonance frequency of the point-mass or elastic inclusion of case A to case B, it  
 301 can be seen that by increasing the distance between the inclusion and the rigid backing **that** the peak is  
 302 shifted down in frequency. This behavior can be explained by considering the foam under the inclusion as a  
 303 spring. Therefore, increasing its length leads to a decrease in its stiffness, which results in a lower resonance  
 304 frequency of the mass-spring system.

305 *3.1.3. Sound absorption of meta-poro-elastic systems under oblique incidence angle*

306 To assess the utility of the meta-poro-elastic system in real applications, the performance of the con-  
 307 sidered meta-poro-elastic configurations under oblique incidence angle is evaluated. Figure 7 shows the  
 308 (partial) absorption coefficients calculated for case A and case B under different angles of incidence ( $\theta$ )  
 varying from  $0^\circ$ , i.e. normal incidence, to  $78^\circ$ , i.e. close to grazing incidence.

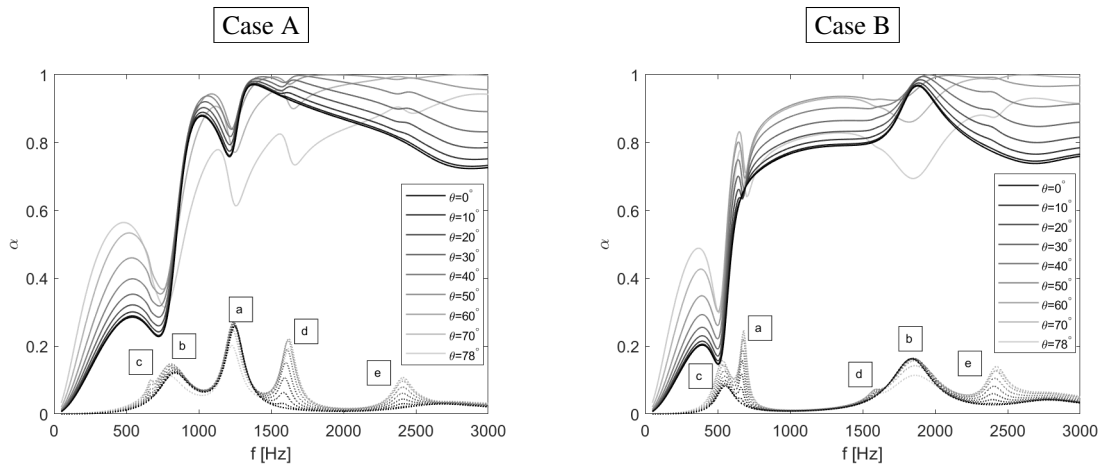


Figure 7: The total absorption coefficient (solid lines) and the partial structural absorption coefficient (dotted lines) of case A and case B with elastic inclusions under oblique incidence angle ( $\theta$ ).

309  
 310 As compared to normal incidence (Figure 4), the absorption curves under oblique incidence (Figure 7)  
 311 show three additional peaks in the structural losses (labeled as c, d, and e in Figure 7) when the incidence  
 312 angle deviates from  $\theta = 0^\circ$ . Recall that the peaks marked with letters a and b correspond to the mass-spring  
 313 effect and the modified mode effect along the  $y$ -axis, respectively. The additional peaks are related to the  
 314 modes excited along the  $x$ -axis by the in-plane component of the incident plane wave. Two of which, i.e. c  
 315 and d, are the modified first- and second-order shear modes due to inclusion, while the other one, i.e. e, is an  
 316 additional mode excited by the inclusion resonating along the  $x$ -axis. The latter has a resonance frequency

317 around 2400 Hz, which is double of the vertical mass-spring resonance for case A around 1250 Hz. This is  
 318 because the horizontal distance of the inclusion ( $L_x = 8$  mm) is double the vertical distance of the inclusion  
 319 from the rigid wall for case A ( $y_A = 4$  mm).

320 To assess the performance of case A and case B (with elastic inclusions) with respect to case 0 in a  
 321 more general setting, the diffuse-field absorption of the two cases are compared to case 0 in Figure 8. This  
 evaluation confirms that the mass-spring effect is preserved under the assumption of diffuse-field.

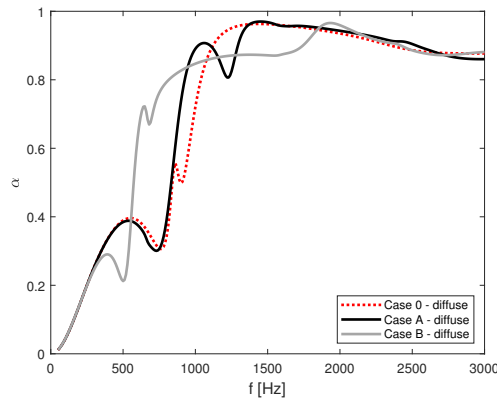


Figure 8: Diffuse-field absorption coefficient of case 0, case A, and case B.

322

### 323 3.2. Mass-spring effect

324 The previous part **demonstrated** that resonant behavior in a meta-poro-elastic system can lead to an  
 325 absorption peak, whether it is by alternating the frame vibration pattern at its first natural frequency or  
 326 by inducing an additional mode in the system, such as the mass-spring effect. This part investigates the  
 327 conditions under which this mass-spring resonance leads to absorption improvement.

#### 328 3.2.1. Dependency on viscous transport parameters

329 The mass-spring effect leads to an increase in the absorption coefficient by forcing the poro-elastic  
 330 skeleton to move out-of-phase with respect to the fluid part due to the resonating inclusion. A larger phase  
 331 difference results in an increase in viscous losses. Therefore, intuitively it is understood that the absorption  
 332 coefficient enhancement due to the mass-spring effect strongly depends on the values of flow resistivity  
 333 ( $\sigma$ ) and viscous characteristic length ( $\Lambda$ ). This statement is **validated** by considering case A and varying  $\sigma$   
 334 and  $\Lambda$  while keeping all the other parameters constant, and **then** plotting the absorption peak values due to  
 335 the mass-spring effect (the local maxima in the absorption curve between the frequencies at which the two

336 structural-loss peaks appear), see Figure 9(a). It is apparent in Figure 9(a) that the increase of absorption  
 337 peak value is more sensitive to changes in the viscous characteristic length as compared to changes in  
 338 the flow resistivity. Additionally, normalised values of the real part of the viscous coupling coefficient,  
 339 i.e.  $\text{Re}(\tilde{b}/(\omega\rho_a))$  see equation (5), are also calculated at those frequencies, and presented in Figure 6(b) for  
 340 various values of  $\sigma$  and  $\Lambda$ . Recall that the viscous coupling coefficient (5) depends on the dynamic viscous  
 341 tortuosity  $\tilde{\alpha}$ , which depends on  $\sigma$  and  $\Lambda$  according to the Johnson et al. [28, 22] model, and this coefficient  
 342 corresponds to the amount of viscous losses. Note that  $\text{Re}(\tilde{b})$  is used for the plot in Figure 9(b) because  
 343 the real part is associated with the dissipative part of the viscous forces, while the imaginary part  $\text{Im}(\tilde{b})$  is  
 344 associated with the modification of tortuosity due to the added mass effect related to the viscous behaviour  
 345 of the fluid in the pores [27]. From the graphs in Figure 9, it can be seen that the mass-spring effect can  
 346 occur in all types of poro-elastic foams, but that pronounced improvements in absorption only occur in  
 347 foams with high flow resistivity and/or low viscous characteristic length (cf. white and light-gray areas in  
 348 Figure 9).

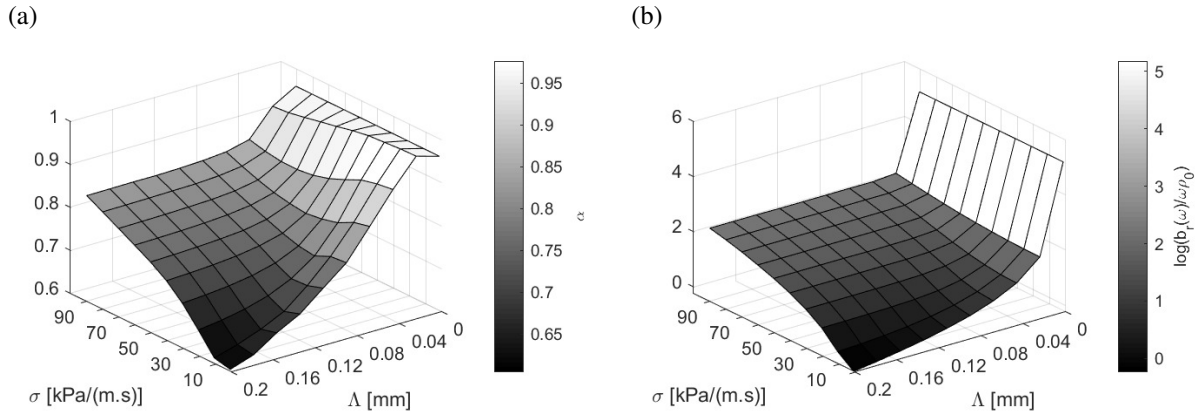


Figure 9: The value of the absorption coefficient peak due to the mass-spring effect (a) and the value of normalised viscous coupling coefficient at the absorption peak frequencies (b) for different combinations of viscous characteristic length and flow resistivity.

### 349 3.2.2. Dependency on inclusion properties

350 The size and mass of the inclusion impact both the total absorption coefficient and the mass-spring  
 351 effect. To verify their effect, an investigation is carried out in three steps. In the first step, the effect of the  
 352 inclusion mass is investigated by keeping the size of the inclusion constant ( $r = 0.4$  mm) and increasing  
 353 its mass density. In the second step, in order to isolate the effect of inclusion size the inclusion mass is kept  
 354 constant and equal to that of a steel rod of radius  $r = 0.4$  mm, while the inclusion size is increased. In the  
 355 third step, the combined effect of size and mass is evaluated by increasing the elastic inclusion size.

356 *I. The effect of inclusion mass*

357 In the first step, the effect of the inclusion mass is investigated by considering the elastic inclusion of case  
 358 A and case B and increasing its mass density such that the inclusion mass ( $m$ ) is equal to the mass ( $m_r$ ) of  
 359 a steel rod with radius  $r_{eq} = 0.2, 0.4, 0.8, 1.2, \dots, 3.6$  mm, while keeping the inclusion size constant and  
 360 equal to  $r = 0.4$  mm. The total absorption coefficients, as well as the partial absorption coefficients due to  
 361 structural losses, are compared in Figure 10 for the considered values of the inclusion mass. Additionally,  
 362 the blue line in Figure 10 is the projection of the first structural losses peak on the  $f - r_{eq}$  plane. Similarly,  
 363 the red line is the projection of the second absorption peak on the  $f - r_{eq}$  plane. Moreover, the red and blue  
 364 dots are the values of total absorption at these structural peaks.

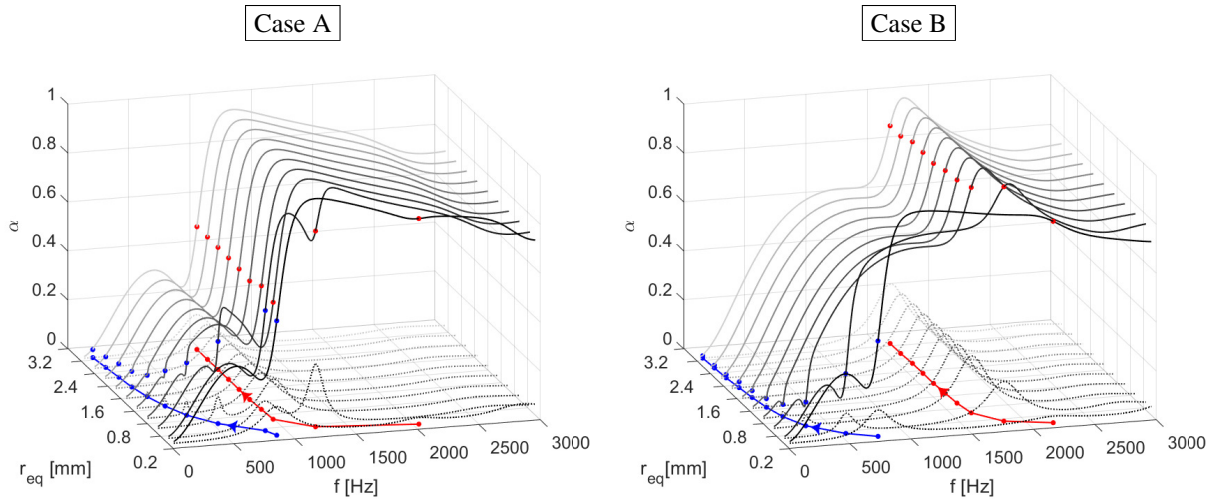


Figure 10: The total absorption (black and gray continuous curves) and partial absorption due to structural losses (black and gray dotted curves) for poro-elastic cells containing an elastic rod inclusion with the same radius  $r = 0.4$  mm and various masses ( $m$ ) equivalent to the mass ( $m_r$ ) of an inclusion with a radius of  $r = r_{eq}$  in millimeter.

365 Considering both cases, it is clear that both the mass-spring resonance frequency (the blue line) and  
 366 the resonance frequency of the frame (the red line) are shifted down in frequency when the inclusion mass  
 367 is increased. For both cases, above a certain amount of mass addition (i.e.  $m_{1.6}$ ), the observed behavior  
 368 converges asymptotically as the mass increases. This means that the mass-spring resonance frequency  
 369 converges to zero for heavy inclusions, and the inclusion only modifies the mode of frame. Moreover, the  
 370 value of the peak in structural losses due to inclusion resonance decreases as it is shifted down in frequency  
 371 since at lower frequencies fewer cycles per second occur and hence less energy is dissipated.

## 372 II. The effect of inclusion size

373 The influence of different inclusions sizes, while keeping mass fixed, is shown in Figure 11. It can be seen  
374 that the resonance frequency of the inclusion (the blue curve), increases for larger inclusion sizes, and hence  
375 follows the opposite trend as for the previous study illustrated in Figure 10. This is explained by the fact  
376 that increasing the size of inclusion leads to an increase in the effective area of the spring and a decrease  
377 in the effective length of the spring [35]; thus, the spring stiffness is increased while the mass remains the  
378 same which increases the mass-spring resonance frequency. Similarly, the resonance frequency of the frame  
379 (the red curve) is also shifted up in frequency. The shift in resonance frequency of the frame is due to the  
380 added stiffness to the frame in combination with a decrease in the distance between the inclusion and the  
381 rigid backing as the inclusion dimension increases, which leads to an extended area of rigid-like boundary  
382 condition on the foam and thus increasing the frame resonance frequency.

383 It should be noted that in case B the total absorption coefficient drops significantly for larger inclusions.  
384 This occurs because the inclusion size becomes comparable to or larger than the two longitudinal wave-  
385 lengths, i.e.  $\frac{\lambda}{r} \approx 2$  for  $r = 2.4$  mm at  $f = 1500$  Hz, and it is located very close to the surface. Consequently,  
386 most of the wave is reflected. Additionally, the spacing between the inclusions decreases with the increase  
387 in the inclusion size (because the width of the periodic cell remains the same), leading to a decrease in the  
388 material that the sound wave can propagate through and be dissipated.

389 It can be seen that the peaks due to the mass-spring resonance are more pronounced for larger inclusions.  
390 This is related to the fact that when the size of the inclusion is increased, the added mass is distributed over  
391 a larger area, therefore it affects a wider area of the foam around it, i.e. increase in the frame displacement  
392 which corresponds to a higher peak in the structural loss. Additionally, the resonance frequency of the  
393 inclusion is shifted higher in frequency, where more cycles per second occur and hence more energy can be  
394 dissipated.

395 To demonstrate the former, the field variables (i.e. the solid phase displacements, the fluid phase dis-  
396 placements, and the pressure) at the inclusion resonance frequency (800 Hz) are shown for the smallest and  
397 the largest inclusions in Figure 12, where the real part of the solid displacement along the  $x$ -axis and along  
398 the  $y$ -axis, and the real part of the pore pressure are denoted by  $u$ ,  $v$ , and  $p$ , respectively. The real part  
399 of the fluid displacement along the  $x$ -axis and along the  $y$ -axis are indicated with  $u^f$  and  $v^f$ , respectively.  
400 Figure 12 shows that at  $f = 800$  Hz for both cases the frame is excited by the resonating inclusion to move  
401 out-of-phase with the fluid phase and it is clear that the area of the poro-elastic layer affected by the large

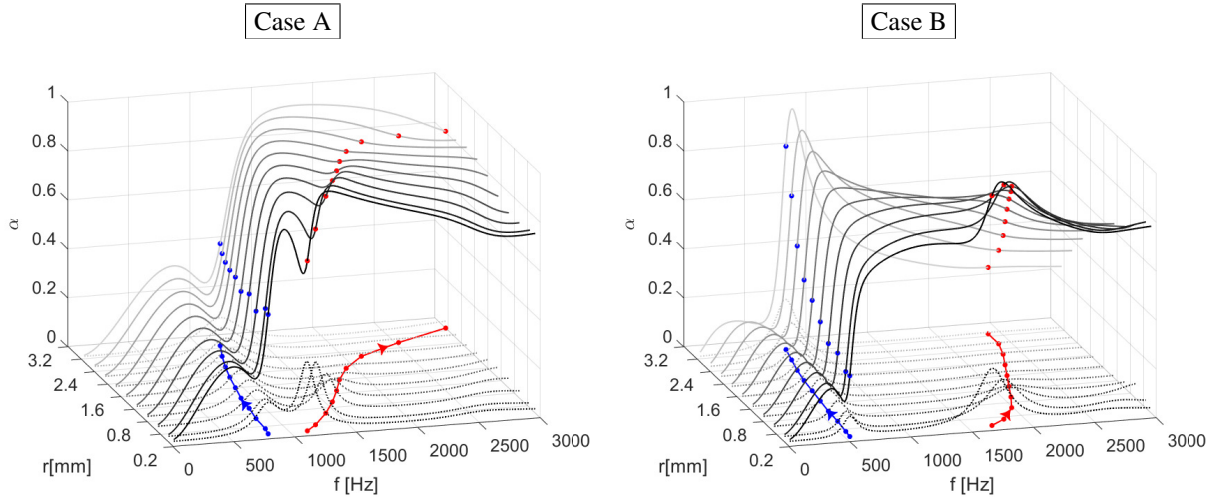


Figure 11: The total absorption (black and gray continuous curves) and partial absorption due to structural losses (black and gray dotted curves) for poro-elastic cells containing an elastic inclusion with various radii  $r$ , but constant mass equal to that of a steel rod with a radius 0.4 mm.

402 inclusion is larger than the area affected by the small inclusion.

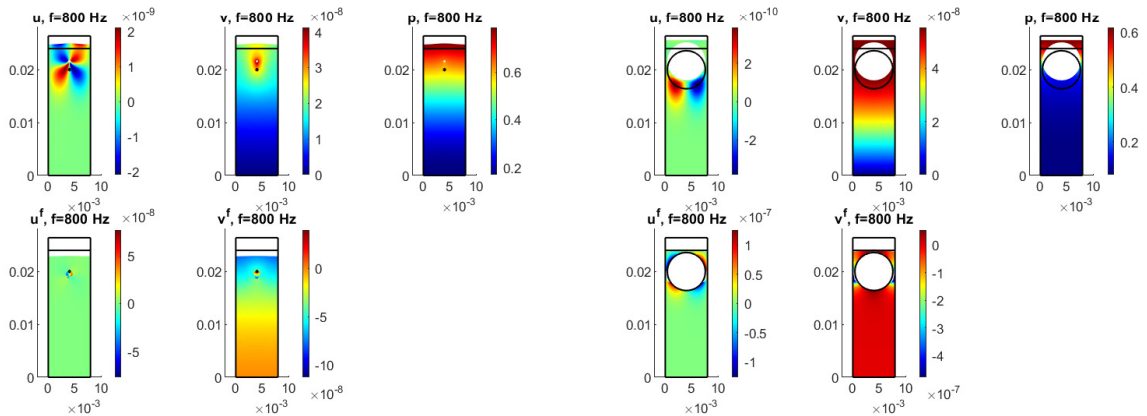


Figure 12: The field variables at  $f = 800$  Hz in the poro-elastic layer with elastic inclusion with a radius of  $r = 0.2$  mm (graphs on the left) or 3.6 mm (graphs on the right).

403 *III. The combined effect of the inclusion mass and size*

404 To conclude this study on the influence of geometry, **the radius of, and accordingly the mass of, the steel**  
 405 **inclusion is varied.** The total absorption, as well as the partial absorption coefficients due to structural  
 406 losses, are shown in Figure 13 for both cases A and B.

407 Considering case A it is apparent that by increasing the diameter of the inclusion, and consequently  
 408 the added mass, the mass-spring resonance (the blue line) is shifted down in frequency (from 1920 Hz to

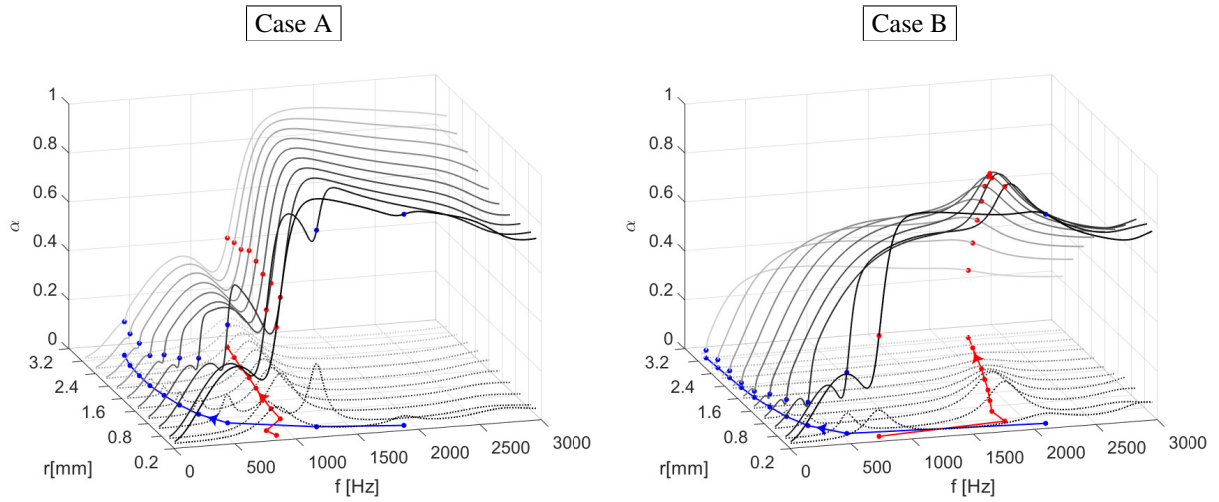


Figure 13: The total absorption (black and gray continuous curves) and partial absorption due to structural losses (black and gray dotted curves) for poro-elastic cells containing a steel rod inclusion of different radii.

320 Hz), while the resonance frequency of the frame (the red line) is shifted up in frequency (from 890 Hz  
to 1210 Hz). The value of the peak in structural losses due to the mass-spring resonance decreases since  
the larger inclusion rigidifies the foam and also in lower frequencies the energy dissipation decreases due to  
fewer cycles per second. It should be noted that the shift in resonance frequency of the mass-spring system  
is due to the increase in added mass, which is more dominant than the increase in the effective area and  
decrease in the effective length of the spring acting underneath the inclusion. The shift in the resonance  
frequency of the frame follows the same trend as in the previous study. For very small inclusions (i.e.  
 $r = 0.2$  mm and  $r = 0.4$  mm) the resonance frequency of the frame is lower than that of the inclusion  
(therefore, the red and blue curves intersect).

All remarks explained above can be observed more clearly in case B (Figure 13(right)) since the reso-  
nance frequency of the mass-spring system and frame are located further apart. In this case, the mass-spring  
resonance frequency lowers from 2100 Hz to 80 Hz, and at the same time the frame resonance frequency  
shifts up from 770 Hz to 2160 Hz.

### 3.3. Tunability of the mass-spring effect

As a final study the combined effect of the inclusions size and location is investigated in order to find  
the optimal absorption that can be achieved at various frequencies. To do so, an optimization problem is  
defined with a design space consisting of the inclusion radius ( $r$ ) and the vertical position of the inclusion  
( $y$ ). These parameters are optimized at each frequency such that a curve indicating the maximal achievable

427 absorption is obtained. The following objective function is used:

$$f_p = |1 - \alpha|^2. \quad (10)$$

428 The presented optimization problem is solved using the *patternsearch* function in Matlab [36, 37]. It should  
 429 be mentioned that the elastic inclusion model is used in the optimization problem.

430 Figure 14 summarizes the results of this optimization routine. The optimized parameter values at the  
 431 targeted frequencies between 100 Hz and 3000 Hz are shown in Figure 14(b), while the best feasible ab-  
 432 sorption coefficient values, by using the optimized parameters at each frequency, are marked with red circles  
 433 in Figure 14(a).

434 Two different trends in the design parameters progression over two frequency ranges are observed and  
 435 marked in white in Figure 14(b). The first frequency range, from 500 Hz to 900 Hz, is the mass-spring dom-  
 436 inated region, while the second one, from 1700 Hz to 3000 Hz, is dominated by the modified mode effect.  
 437 In the first frequency range, the absorption enhancement is due to the mass-spring effect and the resonance  
 438 frequency has a negative relation with the inclusion size and its (absolute) position from the rigid backing.  
 439 Moreover, Figure 14(b) shows that (in this region) the size of the inclusion should be deep-subwavelength  
 440 since there is a drop in inclusion size from sub-wavelength scale ( $\frac{\lambda}{r} \approx 40$ ) to deep-subwavelength ( $\frac{\lambda}{r} \approx 200$ )  
 441 at 500 Hz, where the mass-spring effect dominated region begins.

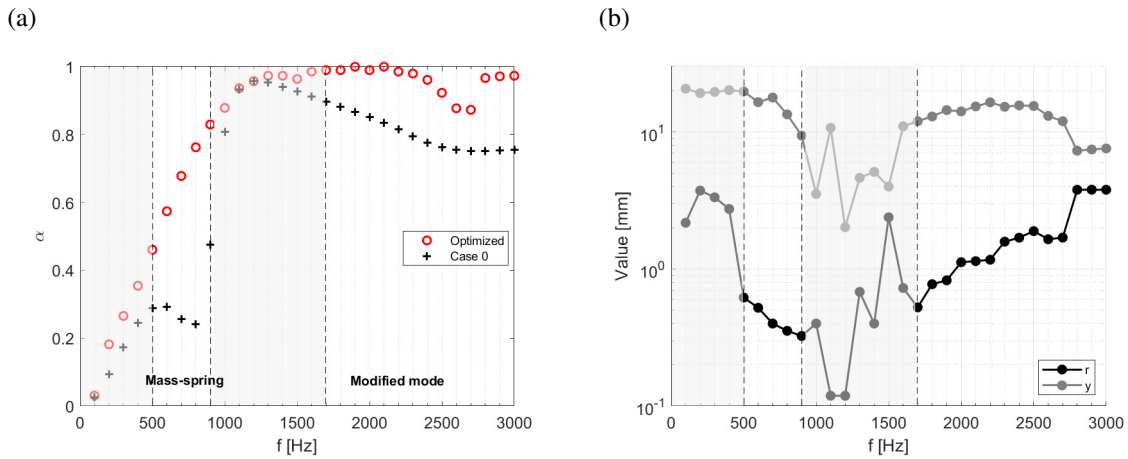


Figure 14: The absorption coefficient at the targeted frequencies of the optimization (a), and the converged values of the design space parameters (b). The red circles in the left plot refer to the best absorption coefficient value that can be obtained at each targeted frequency using the parameters shown in the right plot at that specific frequency.

442 In the second region, i.e. the modified mode dominated region, the frequency has a positive relation

443 with the inclusion size. The reason for this is that the larger inclusion stiffens the foam and shifts the mode  
444 of the frame to a higher frequency. However, the optimal inclusion position does not seem to be strongly  
445 dependent on the frequency at which it is optimised and it seems that the optimal position of the inclusion  
446 is approximately in the middle of the foam layer for all the frequencies in the modified mode dominated  
447 region.

448 There is a transition zone between the two regions (the gray area from 900 Hz to 1600 Hz), where the  
449 choice of the design parameters seems to be more random. This zone starts around the natural mode of the  
450 frame in case 0, i.e. at  $f_r \approx 820$  Hz. Inside this zone, the design parameters cannot be optimized because:  
451 (i) the inclusion is already at the lowest vertical position and lowest dimension possible, therefore the mass-  
452 spring effect has reached its limit; (ii) the modified mode is always higher in frequency as compared to  
453 the natural mode of the frame and there will be always a minimum frequency offset between them. This  
454 minimum frequency offset corresponds to unit cell characteristic length which is fixed in this case. All this  
455 results in a transition zone that is neither dominated by the mass-spring effect nor by the modified mode  
456 effect.

#### 457 **4. Conclusions**

458 In this paper the absorption of poro-elastic material is enhanced in the viscous regime using a mass-  
459 spring effect. It is shown that by embedding a deep-subwavelength inclusion in a poro-elastic layer a mass-  
460 spring system can be induced, where the foam under the inclusion acts as a spring. Therefore, by tweaking  
461 the added mass and its distance from the rigid backing the resonance frequency of the system can be tuned.  
462 More specifically, the resonance frequency of the mass-spring system has an inverse relation with both  
463 of these parameters. Moreover, it is shown that the resonating inclusion excites the out-of-phase motion  
464 between the fluid and solid phase of the porous material leading to an increase in the energy dissipation  
465 due to viscous effects. This phenomenon is apparent for the poro-elastic material under the decoupling  
466 frequency and when the inclusion is fully coupled to the poro-elastic domain or at least modeled as a point-  
467 mass inclusion. The mass-spring effect is **identified** by decomposing the absorption coefficient in three  
468 energy dissipation **mechanisms**, viz. viscous, thermal, and structural, for three different cases of poro-elastic  
469 layers, namely, without inclusion and with inclusion at two different locations (i.e. close to the rigid backing  
470 or layer surface). It is shown that the peaks in the absorption curve correspond to the increase in out-of-  
471 phase movement of the two phases, which happens at the resonance frequency of the mass-spring system

472 and the resonance frequency of the frame. This explains that the mass-spring effect increases the viscous  
473 energy dissipation by forcing the frame to move out-of-phase with the fluid part. After elaboration on  
474 the resonant behaviors in the proposed meta-poro-elastic systems, the physical and geometrical parameters  
475 that intensify or degrade the mass-spring effect were discussed. It was demonstrated that, since the mass-  
476 spring effect enhances the absorption coefficient through viscous losses, the poro-elastic layer should have  
477 a relatively high viscous energy dissipation at low frequencies. This translates into a high value of the  
478 flow resistivity and/or a low value of the viscous characteristic length. Additionally, it was shown that the  
479 size of the inclusion plays an important role in the effectiveness of the meta-poro-elastic system: when the  
480 inclusion size becomes comparable to the wavelength in the medium, the inclusion stiffens the foam around  
481 it leading to either extension of the rigid backing or reflection of the incidence wave from the surface by  
482 the large inclusion depending on its location. Finally, it is shown that the mass-spring effect increases the  
483 absorption coefficient in the viscous regime, even for an oblique angle of incidence. Therefore, this work  
484 presents the potential of this effect as an absorption enhancement strategy in poro-elastic materials with a  
485 high decoupling frequency.

## 486 Acknowledgements

487 The European Commission is gratefully acknowledged for their support of the VIPER research project  
488 (GA 675441). The Research Fund KU Leuven is gratefully acknowledged for its support. The research of  
489 E. Deckers is funded by a grant from the Research Foundation – Flanders (FWO). This research was partially  
490 supported by Flanders Make, the strategic research centre for the manufacturing industry. T. G. Zieliński  
491 and Ł. Jankowski would like to acknowledge the financial support from the National Science Centre (NCN),  
492 Poland, under Grant Agreement No. 2015/19/B/ST8/03979.

## 493 Appendix A. Weak forms

494 The weak integral formulation of the Helmholtz equation for the acoustic pressure  $p$  inside the acoustic  
495 domain  $\Omega_a$  reads:

$$-\int_{\Omega_a} \frac{1}{\omega^2 \rho_a} \nabla \bar{q} \cdot \nabla p \, d\Omega_a + \int_{\Omega_a} \frac{1}{K_a} \bar{q} p \, d\Omega_a + \int_{\Gamma_a} \frac{1}{\omega^2 \rho_a} \bar{q} \nabla p \cdot \mathbf{n} \, d\Gamma_a = 0, \quad (\text{A.1})$$

496 where  $\rho_a$  and  $K_a$  are the density and bulk modulus of air,  $\Gamma_a$  is the Neumann-type boundary,  $\mathbf{n}$  is the  
497 outward unit vector to normal to it, while  $q$  and  $\bar{q}$  are the test function for  $p$  and its complex conjugate. Con-

498 sidering a periodic solution to the problem of equation (A.1), the problem description can be reformulated  
 499 as follows:

$$\mathcal{WF}_a = - \int_{\Omega_a} \frac{1}{\omega^2 \rho_a} \bar{\nabla} \bar{q} \cdot \hat{\nabla} \hat{p} \, d\Omega_a + \int_{\Omega_a} \frac{1}{K_a} \bar{q} \hat{p} \, d\Omega_a + \int_{\Gamma_a} \frac{1}{\omega^2 \rho_a} \bar{q} \hat{\nabla} \hat{p} \cdot \mathbf{n} \, d\Gamma_a = 0, \quad (\text{A.2})$$

500 where  $\hat{p} = p \exp(i\tilde{\mathbf{k}} \cdot \mathbf{x})$  and  $\bar{q} = \bar{q} \exp(-i\tilde{\mathbf{k}} \cdot \mathbf{x})$  are the periodic pressure field and the corresponding test  
 501 function. Here and below,  $\bar{\nabla} = \nabla - i\tilde{\mathbf{k}}$  and  $\hat{\nabla} = \nabla + i\tilde{\mathbf{k}}$  are the shifted gradient operators for the test functions  
 502 and field variables, respectively.

503 The weak formulation for the poro-elastic domain  $\Omega_p$  can be reformulated in the same manner as for  
 504 the acoustic domain by considering periodic representations  $\hat{p}$  and  $\hat{\mathbf{u}} = \mathbf{u} \exp(i\tilde{\mathbf{k}} \cdot \mathbf{x})$  of the pore pressure  $p$   
 505 and solid phase displacements  $\mathbf{u}$ , respectively, namely:

$$\begin{aligned} \mathcal{WF}_p = & \int_{\Omega_p} \omega^2 \tilde{\rho} \hat{\mathbf{u}} \cdot \bar{\mathbf{w}} \, d\Omega_p - \int_{\Omega_p} \hat{\boldsymbol{\sigma}}(\hat{\mathbf{u}}) \bullet \bar{\nabla} \bar{\mathbf{w}} \, d\Omega_p + \int_{\Omega_p} (\tilde{\gamma} + \tilde{\xi}) \bar{\nabla} \hat{p} \cdot \bar{\mathbf{w}} \, d\Omega_p + \int_{\Omega_p} \tilde{\xi} \hat{p} \bar{\nabla} \cdot \bar{\mathbf{w}} \, d\Omega_p \\ & - \int_{\Omega_p} \frac{\phi^2}{\omega^2 \tilde{\rho}_{22}} \bar{\nabla} \hat{p} \cdot \bar{\nabla} \bar{q} \, d\Omega_p + \int_{\Omega_p} \frac{\phi^2}{\tilde{R}} \hat{p} \bar{q} \, d\Omega_p + \int_{\Omega_p} (\tilde{\gamma} + \tilde{\xi}) \hat{\mathbf{u}} \cdot \bar{\nabla} \bar{q} \, d\Omega_p + \int_{\Omega_p} \tilde{\xi} \bar{\nabla} \cdot \hat{\mathbf{u}} \bar{q} \, d\Omega_p = 0, \end{aligned} \quad (\text{A.3})$$

506 where  $\bullet$  denotes the scalar product of second order tensors,  $\tilde{\xi} = \phi(1 + \tilde{Q}/\tilde{R})$ , and  $\bar{\mathbf{w}} = \bar{\mathbf{w}} \exp(-i\tilde{\mathbf{k}} \cdot \mathbf{x})$  is the  
 507 periodic test function for  $\hat{\mathbf{u}}$ . Moreover, the stress tensor depends only on the periodic displacement field of  
 508 solid phase, namely,

$$\hat{\boldsymbol{\sigma}} = \hat{A} (\bar{\nabla} \cdot \hat{\mathbf{u}}) \mathbf{I} + \tilde{N} (\bar{\nabla} \hat{\mathbf{u}} + \bar{\nabla}^T \hat{\mathbf{u}}). \quad (\text{A.4})$$

509 Similarly, the weak formulation for the periodic field representation of the elastic domain  $\Omega_e$  can be  
 510 written as:

$$\mathcal{WF}_e = \int_{\Omega_e} \omega^2 \rho_e \hat{\mathbf{u}} \cdot \bar{\mathbf{w}} \, d\Omega_e - \int_{\Omega_e} \hat{\boldsymbol{\sigma}}_e(\hat{\mathbf{u}}) \bullet \bar{\nabla} \bar{\mathbf{w}} \, d\Omega_e = 0, \quad (\text{A.5})$$

511 where  $\rho_e$  is the mass density of elastic material, while the periodic field of elastic stress tensor  $\hat{\boldsymbol{\sigma}}_e$  depends  
 512 on  $\hat{\mathbf{u}}$  and the Lamé coefficients  $\lambda_e$  and  $\mu_e$  of the isotropic material of inclusions as follows

$$\hat{\boldsymbol{\sigma}}_e = \lambda_e (\bar{\nabla} \cdot \hat{\mathbf{u}}) \mathbf{I} + \mu_e (\bar{\nabla} \hat{\mathbf{u}} + \bar{\nabla}^T \hat{\mathbf{u}}). \quad (\text{A.6})$$

513 It should be noted that we have skipped surface integrals in the weak formulation of poro-elasticity (A.3)  
 514 and elasticity (A.5), because they are irrelevant for the configuration analysed in this work. Moreover, in  
 515 this formulation the coupling on the interface between the poro-elastic and elastic media is natural, and

516 since the elastic inclusion is embedded in the poro-elastic domain and has no direct contact with air the only  
 517 non-zero coupling integral appears on the interface between the acoustic and poro-elastic domains:

$$IC_{p-a} = \int_{\Gamma_{p-a}} \hat{\mathbf{u}} \cdot \mathbf{n} \bar{q} \, d\Gamma_{p-a} + \int_{\Gamma_{p-a}} \hat{p} \mathbf{n} \cdot \bar{\mathbf{w}} \, d\Gamma_{p-a}, \quad (\text{A.7})$$

518 Thus, the weak formulation for the whole coupled system is:  $\mathcal{WF}_a + \mathcal{WF}_p + \mathcal{WF}_e + IC_{p-a} = 0$ .

## 519 References

- 520 [1] L. M. Brekhovskikh, *Waves in Layered Media*, Second Edition, Elsevier, 1980.
- 521 [2] J.-P. Groby, A. Wirgin, L. De Ryck, W. Lauriks, R. P. Gilbert, Y. S. Xu, Acoustic response of a rigid-frame porous medium  
 522 plate with a periodic set of inclusions, *J. Acoust. Soc. Am.* 126 (2) (2009) 685–693. doi:10.1121/1.3158936.  
 523 URL <https://doi.org/10.1121/1.3158936>
- 524 [3] J.-P. Groby, O. Dazel, A. Duclos, L. Boeckx, L. Kelders, Enhancing the absorption coefficient of a backed rigid frame porous  
 525 layer by embedding circular periodic inclusions, *J. Acoust. Soc. Am.* 130 (6) (2011) 3771–3780. doi:10.1121/1.3652865.  
 526 URL <http://asa.scitation.org/doi/10.1121/1.3652865>
- 527 [4] C. Lagarrigue, J. P. Groby, V. Tournat, O. Dazel, O. Umnova, Absorption of sound by porous layers with embedded periodic  
 528 arrays of resonant inclusions, *J. Acoust. Soc. Am.* 134 (6) (2013) 4670–4680. doi:10.1121/1.4824843.  
 529 URL <http://asa.scitation.org/doi/10.1121/1.4824843>
- 530 [5] A. Krynkin, O. Umnova, A. Y. B. Chong, S. Taherzadeh, K. Attenborough, Scattering by coupled resonating elements in air,  
 531 *J. Phys. D* 44 (12) (2011) 125501.
- 532 [6] J.-P. Groby, C. Lagarrigue, B. Brouard, O. Dazel, V. Tournat, B. Nennig, Enhancing the absorption properties of acoustic  
 533 porous plates by periodically embedding Helmholtz resonators, *J. Acoust. Soc. Am.* 137 (2015) 273. doi:10.1121/1.4904534.  
 534 URL <https://doi.org/10.1121/1.4904534>
- 535 [7] T. Weisser, J.-P. Groby, O. Dazel, F. Gaultier, E. Deckers, S. Futatsugi, L. Monteiro, Acoustic behavior of a rigidly backed  
 536 poroelastic layer with periodic resonant inclusions by a multiple scattering approach, *J. Acoust. Soc. Am.* 139 (2) (2016)  
 537 617–629. doi:10.1121/1.4940669.  
 538 URL <http://asa.scitation.org/doi/10.1121/1.4940669>
- 539 [8] T. G. Zieliński, Modelling of poroelastic layers with mass implants improving acoustic absorption, in: *Proceedings of*  
 540 *ICA2007 – 19th International Congress on Acoustics, 2-7 September 2007, Madrid, Spain, 2007*.
- 541 [9] M. R. F. Kidner, C. R. Fuller, B. Gardner, Increase in transmission loss of single panels by addition of mass inclusions to a  
 542 poro-elastic layer: Experimental investigation, *J. Sound Vib.* 294 (3) (2006) 466–472. doi:10.1016/J.JSV.2005.11.022.  
 543 URL <https://www.sciencedirect.com/science/article/pii/S0022460X05007765>
- 544 [10] T. G. Zieliński, Numerical investigation of active porous composites with enhanced acoustic absorption, *J. Sound Vib.*  
 545 330 (22) (2011) 5292–5308.
- 546 [11] T. G. Zieliński, M.-A. Galland, E. Deckers, Influencing the wave-attenuating coupling of solid and fluid phases in poroe-  
 547 lastic layers using piezoelectric inclusions and locally added masses, in: W. Desmet, B. Pluymers, D. Moens, W. Rottiers

- 548 (Eds.), Proceedings of ISMA2018 International Conference on Noise and Vibration Engineering and USD2018 International  
549 Conference on Uncertainty in Structural Dynamics, 2018, pp. 1091–1103.
- 550 [12] M. A. Lewińska, J. A. van Dommelen, V. G. Kouznetsova, M. G. Geers, Towards acoustic metafoams: The en-  
551 hanced performance of a poroelastic material with local resonators, *J. Mech. Phys. Solids* 124 (2019) 189–205.  
552 doi:10.1016/j.jmps.2018.10.006.  
553 URL [www.elsevier.com/locate/jmps](http://www.elsevier.com/locate/jmps)
- 554 [13] M. A. Lewińska, J. A. van Dommelen, V. G. Kouznetsova, M. G. Geers, Broadening the attenuation range of acoustic  
555 metafoams through graded microstructures, *J. Sound Vib.* 483 (2020) 115472. doi:10.1016/j.jsv.2020.115472.  
556 URL <https://doi.org/10.1016/j.jsv.2020.115472>
- 557 [14] B. Nennig, Y. Renou, J.-P. Groby, Y. Aurégan, A mode matching approach for modeling two dimensional porous grating with  
558 infinitely rigid or soft inclusions, *The Journal of the Acoustical Society of America* 131 (5) (2012) 3841–3852.
- 559 [15] C. Lagarrigue, J. P. Groby, O. Dazel, V. Tournat, Design of metaporous supercells by genetic algorithm for absorption  
560 optimization on a wide frequency band, *Appl. Acoust.* 102 (2016) 49–54. doi:10.1016/j.apacoust.2015.09.011.  
561 URL <http://dx.doi.org/10.1016/j.apacoust.2015.09.011>
- 562 [16] L. Feng, Enhancement of low frequency sound absorption by placing thin plates on surface or between layers of porous  
563 materials, *The Journal of the Acoustical Society of America* 146 (2) (2019) EL141–EL144.
- 564 [17] C. Boutin, Acoustics of porous media with inner resonators, *J. Acoust. Soc. Am.* 134 (6) (2013) 4717–4729.
- 565 [18] C. Boutin, F.-X. Bécot, Theory and experiments on poro-acoustics with inner resonators, *Wave Motion* 54 (2015) 76–99.
- 566 [19] X.-F. Zhu, S.-K. Lau, Z. Lu, W. Jeon, Broadband low-frequency sound absorption by periodic metamaterial resonators  
567 embedded in a porous layer, *J. Sound Vib.* 461 (2019) 114922.
- 568 [20] M. A. Biot, Theory of elastic waves in a fluid-saturated porous solid. I. Low frequency range, *J. Acoust. Soc. Am.* 28 (1956)  
569 168–178.
- 570 [21] M. A. Biot, Theory of propagation of elastic waves in a fluid-saturated porous solid. II. Higher frequency range, *J. Acoust.*  
571 *Soc. Am.* 28 (2) (1956) 179–191.
- 572 [22] J. Allard, N. Atalla, Propagation of sound in porous media: modelling sound absorbing materials. Second Edition, John Wiley  
573 & Sons, 2009.
- 574 [23] N. Atalla, R. Panneton, P. Debergue, A mixed displacement-pressure formulation for poroelastic materials, *J. Acoust. Soc.*  
575 *Am.* 104 (1998) 1444. doi:10.1121/1.424355.  
576 URL <https://doi.org/10.1121/1.424355>
- 577 [24] N. Atalla, M. A. Hamdi, R. Panneton, Enhanced weak integral formulation for the mixed (u,p) poroelastic equations, *J.*  
578 *Acoust. Soc. Am.* 109 (6) (2002) 3065–3068. doi:10.1121/1.1365423.  
579 URL <https://doi.org/10.1121/1.1365423>
- 580 [25] M. A. Biot, The elastic coefficients of the theory of consolidation, *J. Appl. Mech.* 15 (1957) 594–601.
- 581 [26] E. Deckers, S. Jonckheere, D. Vandepitte, W. Desmet, Modelling techniques for vibro-acoustic dynamics of poroelastic  
582 materials, *Arch. Computat. Methods. Eng.* 22 (2) (2015) 183–236.
- 583 [27] O. Dazel, F. Sgard, F.-X. Bécot, N. Atalla, Expressions of dissipated powers and stored energies in poroelastic media modeled  
584 by {u, U} and {u, P} formulations, *The Journal of the Acoustical Society of America* 123 (4) (2008) 2054–2063.
- 585 [28] D. L. Johnson, J. Koplik, R. Dashen, Theory of dynamic permeability and tortuosity in fluid-saturated porous media, *J. Fluid*

586 Mech. 176 (1987) 379–402.

587 [29] Y. Champoux, J.-F. Allard, Dynamic tortuosity and bulk modulus in air-saturated porous media, *J. Appl. Phys.* 70 (4) (1991)  
588 1975–1979.

589 [30] P. Debergue, R. Panneton, N. Atalla, Boundary conditions for the weak formulation of the mixed (u, p) poroelasticity problem,  
590 *J. Acoust. Soc. Am.* 106 (5) (1999) 2383–2390.

591 [31] J.-P. Groby, C. Lagarrigue, B. Brouard, O. Dazel, V. Tournat, B. Nennig, Using simple shape three-dimensional rigid inclu-  
592 sions to enhance porous layer absorption, *J. Acoust. Soc. Am.* 136 (3) (2014) 1139–1148.

593 [32] M. Collet, M. Ouisse, M. Ruzzene, M. N. Ichchou, Floquet-Bloch decomposition for the computation of disper-  
594 sion of two-dimensional periodic, damped mechanical systems, *Int. J. Solids Struct.* 48 (20) (2011) 2837–2848.  
595 doi:10.1016/j.ijsolstr.2011.06.002.

596 [33] S. Jonckheere, Wave based and hybrid methodologies for vibro-acoustic simulation with complex damping treatments, Ph.D.  
597 thesis, KU Leuven (2015).

598 [34] P. S. Kurzeja, H. Steeb, About the transition frequency in biot’s theory, *The Journal of the Acoustical Society of America*  
599 131 (6) (2012) EL454–EL460.

600 [35] K. Idrisi, M. E. Johnson, D. Theurich, J. P. Carneal, A study on the characteristic behavior of mass inclusions added to a  
601 poro-elastic layer, *J. Sound Vib.* 329 (20) (2010) 4136–4148. doi:10.1016/j.jsv.2010.04.001.

602 [36] C. Audet, J. E. Dennis, Pattern search algorithms for mixed variable programming, *SIAM J. Optim.* 11 (3) (2000) 573–594.  
603 doi:10.1137/S1052623499352024.  
604 URL <https://scholarship.rice.edu/handle/1911/101991>

605 [37] C. Audet, J. E. Dennis, Analysis of generalized pattern searches, *SIAM J. Optim.* 13 (3) (2003) 889–903.  
606 doi:10.1137/S1052623400378742.  
607 URL <http://www.caam.rice.edu/>

608 **List of Tables**

609 1 The Biot parameters of the foam [23] . . . . . 9

610 **List of Figures**

611 1 Schematic view of the cases considered in this paper. . . . . 4

612 2 Partial absorption coefficient for different dissipation mechanisms for the poro-elastic foam without  
613 inclusions. . . . . 10

614 3 Absorption coefficients calculated for the homogeneous poro-elastic layer using the Biot-JCA (i.e.  
615 Biot-Allard) model and for the corresponding rigid-frame porous layer calculated using the JCA  
616 model of equivalent fluid. . . . . 11

617 4 Total and partial absorption coefficients for case A (a,b,c) and case B (d,e,f), related to different dissi-  
618 pation mechanisms in the poro-elastic layer with the inclusion modeled as rigid (a,d), point mass (b,e)  
619 or elastic (c,f). . . . . 12

620	5	The displacement field (with $v$ referring to the solid displacement along $y$ -axis and $v^f$ referring to the fluid displacement in the same direction) of case A with point-mass inclusion at $f = 820$ Hz (left), and $f = 1250$ Hz (right). These frequencies refer to the peaks in the total absorption coefficient after the mass-spring and frame resonances, respectively. . . . .	13
621			
622			
623			
624	6	The displacement (with $v$ referring to the solid displacement along $y$ -axis and $v^f$ referring to the fluid displacement in the same direction) of case B with point mass inclusion at $f = 1010$ Hz (left), and $f = 1620$ Hz (right). These frequencies refer to the peak in the total absorption coefficient after the mass-spring and frame resonance. . . . .	14
625			
626			
627			
628	7	The total absorption coefficient (solid lines) and the partial structural absorption coefficient (dotted lines) of case A and case B with elastic inclusions under oblique incidence angle ( $\theta$ ). . . . .	15
629			
630	8	Diffuse-field absorption coefficient of case 0, case A, and case B. . . . .	16
631	9	The value of the absorption coefficient peak due to the mass-spring effect (a) and the value of normalised viscous coupling coefficient at the absorption peak frequencies (b) for different combinations of viscous characteristic length and flow resistivity. . . . .	17
632			
633			
634	10	The total absorption (black and gray continuous curves) and partial absorption due to structural losses (black and gray dotted curves) for poro-elastic cells containing an elastic rod inclusion with the same radius $r = 0.4$ mm and various masses ( $m$ ) equivalent to the mass ( $m_r$ ) of an inclusion with a radius of $r = r_{eq}$ in millimeter. . . . .	18
635			
636			
637			
638	11	The total absorption (black and gray continuous curves) and partial absorption due to structural losses (black and gray dotted curves) for poro-elastic cells containing an elastic inclusion with various radii $r$ , but constant mass equal to that of a steel rod with a radius 0.4 mm. . . . .	20
639			
640			
641	12	The field variables at $f = 800$ Hz in the poro-elastic layer with elastic inclusion with a radius of $r = 0.2$ mm (graphs on the left) or 3.6 mm (graphs on the right). . . . .	20
642			
643	13	The total absorption (black and gray continuous curves) and partial absorption due to structural losses (black and gray dotted curves) for poro-elastic cells containing a steel rod inclusion of different radii. . . . .	21
644			
645	14	The absorption coefficient at the targeted frequencies of the optimization (a), and the converged values of the design space parameters (b). The red circles in the left plot refer to the best absorption coefficient value that can be obtained at each targeted frequency using the parameters shown in the right plot at that specific frequency. . . . .	22
646			
647			
648			